Article

Mechanical Behavior of Additive Manufacturing (AM) and Wrought Ti6AI4V with a Martensitic Microstructure

Sara Ricci and Gianluca Iannitti

Special Issue

Processing Technology and Properties of Light Metals

Edited by
Dr. Andrii Kostryzhev and Dr. Olexandra O. Marenych

Article

Mechanical Behavior of Additive Manufacturing (AM) and Wrought Ti6Al4V with a Martensitic Microstructure

Sara Ricci [ID] and Gianluca Iannitti *[ID]

Department of Civil and Mechanical Engineering, University of Cassino and Southern Lazio, 03043 Cassino, FR, Italy; sara.ricci@unicas.it
* Correspondence: g.iannitti@unicas.it

Abstract: Processing and microstructure are fundamental in shaping material behavior and failure characteristics. Additively manufactured materials, due to the rapid heating and solidification process, exhibit unique microstructures compared to their as-cast counterparts, resulting in distinct material properties. In this work, the response of the titanium alloy Ti6Al4V has been investigated for different processing conditions through quasi-static testing. AM Ti6Al4V was fabricated by employing Selective Laser Sintering (SLS) and Selective Laser Melting (SLM) techniques. Both materials present a similar microstructure consisting of an acicular martensitic α'-phase. Commercial Ti6Al4V-grade 5 (supplied as bars) was also examined after heat treatment to achieve a microstructure akin to the AM material. The heat treatment involved rapid heating above the β-phase region and water quenching to obtain a full martensite microstructure. A similar constitutive behavior and tensile–compressive asymmetry in strength were noted for the investigated materials. However, AM alloys exhibited a significantly higher deformation at failure, reaching nearly 40%, compared to only 6.1% for the wrought martensitic material, which can be attributed to the dissimilar distribution of both α' laths and prior-β grain boundaries in the investigated materials. The results indicate that AM can be implemented for the fabrication of martensitic microstructures with mechanical properties superior to those obtained with conventional water-quenching.

Keywords: Ti6Al4V alloy; martensite α'; Selective Laser Melting; Selective Laser Sintering; mechanical properties

1. Introduction

Interest in Additive Manufacturing (AM) technologies has been growing exponentially in recent decades. The great advantages of a layer-by-layer deposition technique, such as on-demand part production and the fabrication of lightweight components with optimized performance, are particularly beneficial in industries such as aerospace and defense, where weight reduction and high performance are critical, or in biomedical applications, where personalized medical devices and implants can be created to meet individual patient needs [1,2]. Titanium alloy Ti6Al4V is one of the most extensively studied materials in the context of additive manufacturing due to its high strength-to-weight ratio, corrosion resistance, and biocompatibility [3]. The microstructure and, consequently, material properties of Ti6Al4V can vary significantly depending on the selected heat treatments [4–8]. In the conventional alloy, the presence of Al—a α stabilizer—and V—a β stabilizer—promotes the formation of a bi-phase material microstructure mainly composed of HCP-α with intergranular BCC-β [9–11]. However, the peculiarities of AM deposition processes—extremely fast cooling rates, repeated thermal cycles, high peak temperatures, and extremely localized heat adduction [12–15]—result in unique microstructures whose mechanical properties might be dissimilar to those of the material produced by conventional techniques. In Ti6Al4V, the localized and severe cooling rates produce extremely fine metastable acicular α' martensitic microstructures distributed in columnar prior-β grains in the as-built

state [16,17]. The directional growth of prior-β grains is strongly associated with the layer-by-layer manufacturing fashion and with the heat transfer mechanisms developed during deposition [18]. Repeated thermal cycles are also responsible for a complex and hierarchical martensitic microstructure distribution, consisting of primary to quarterly α' lamellae, characterized by high-density dislocations and large numbers of twins [19]. Such finer microstructures lead to higher mechanical strength but lower ductility compared to the conventional counterpart [17,20–22]. For this reason, there has been significant effort in understanding how post-processing heat treatments can be implemented to optimize the response of AM Ti6Al4V. The beneficial effects of post-processing treatments in improving material ductility, together with the decomposition of the α' into a more stable $\alpha + \beta$ structure, has been reported in several studies [16,23,24]. For instance, an increase in ductility and a reduction in strength were reported by Mierzejewska et al. [25] after heat-treating DLMS Ti6Al4V at 850 °C for 2 h. If compared to the as-built martensitic state, the material presented an $\alpha + \beta$ microstructure, and process-induced anisotropy was found to be less present. Lee et al. [26] compared the response of horizontally and vertically printed Ti6Al4V samples in the as-built state and heat-treated to achieve different microstructures, from lamellar $\alpha + \beta$ to cellular $\alpha + \beta + \alpha'$. Their results highlighted that by changing the grain morphology from columnar to equiaxial, material anisotropic properties were reduced. Furthermore, stress-relief treatments favored a higher work-hardening and final elongation by lowering the initially high dislocation density. Depending on the heat treatment temperature, the decomposition of the martensitic phase can be accompanied by the evolution of the prior-β grain morphology. Several authors [16,27,28] reported no change in the morphology of the prior-β structure for sub-β-transus temperatures. However, by increasing the heat treatment temperature, ductility was promoted at the expense of strength. Bai et al. [24] subjected SLM Ti6Al4V to different post-processing heat treatments below and above the β-transus temperature. In the first case, they found that lamellae growth was promoted without significant changes to the prior-β microstructure. In the latter, a more equiaxial β grain structure was obtained. The authors concluded that the morphology of the α structure is the main microstructural feature that influences material response. This is consistent with the analysis of Lu et al. [29], who found that the micro-hardness of AM Ti6Al4V, heat-treated with temperatures ranging from 800 °C to 1000 °C, was strongly influenced by the content of the α' martensite and the laths' thickness. Similarly, by performing a hierarchical tailoring of additive Ti6Al4V by two-stage heat treatments, it was shown that strength is governed by martensite content and lamellae thickness, whereas ductility can be improved by changing the morphology of prior-β grains and α' lath length [30]. The authors showed that, by controlling these features, an optimized response can be achieved. The presence of a very fine martensitic phase also strongly impacts the kinetics of phase transformation. Indeed, Vrancken et al. [31] subjected SLM Ti6Al4V to annealing treatments commonly used on conventional alloys, which resulted in significantly different microstructures from those expected. They demonstrated that the best balance between strength and elongation can be achieved by processing the material below the β-transus temperature, followed by furnace cooling. After this processing cycle, the material response fell within the range prescribed by ASTM standards. From Ganor et al.'s analysis [32], hot isostatic pressing (HIP) cycles can further improve the material performance if compared to vacuum annealing only. The in situ decomposition of the martensitic microstructure can offer new possibilities for tailoring and optimizing material response during fabrication [33,34]. For instance, Zafari et al. [33], by changing process parameters, were able to realize different as-built final microstructures, α', near-α', and lamellar $\alpha + \beta$. They showed that the lower ductility of the near-α' microstructure was related to the presence of an isolated thin β phase, which promoted high stress concentration levels at the $\alpha + \beta$ interface, favoring an accelerated fracture process. Similarly, Xu et al. [34] focused on tailoring the microstructure of SLM Ti6Al4V to improve the performance of horizontally printed samples. By controlling processing parameters, it was possible to achieve partial or total in situ martensite decomposition into an $\alpha + \beta$ structure, promoting material ductility. Thus, it can

be concluded that there is extensive literature on the optimization and tailoring of the AM Ti6Al4V microstructure to obtain a mechanical response akin to the conventional $\alpha + \beta$ alloy. However, limited investigations have been undertaken to compare the responses of the wrought and AM martensite microstructure in Ti6Al4V. Sun et al. [35] investigated the effect of the martensitic microstructure on the deformation mechanisms of Ti6Al4V manufactured by SLM in the as-built and water-quenched states and the wrought water-quenched alloy. Their results highlighted that additive manufacturing enables the production of martensitic microstructures with improved ductility compared to those obtained through conventional water-quenching. From an industrial perspective, printed materials are typically subjected to stress relief heat treatments, which, as mentioned earlier, can have beneficial effects on mechanical properties. In this optic, the following work focuses on comparing the properties of the martensitic Ti6Al4V alloy manufactured through different processes: two additive techniques and the water quenching of the conventional alloy. All three materials have been investigated in the stress-relieved state, and different building orientations have been probed for the AM alloys to evaluate the presence of a process-induced anisotropic behavior. Hardness measurement, quasi-static tensile tests at different temperatures and strain rates, and compressive tests have been performed to quantitatively assess how the processing route influences strength and ductility but also to qualitatively investigate and compare the main characteristics of material plastics and constitutive response in the quasi-static regime. The results demonstrate a notable improvement in the mechanical properties of the Ti6Al4V alloy produced via AM compared to the wrought material with a similar microstructure under different loading conditions, temperatures, and strain rates.

2. Materials and Methods

2.1. Materials

The present study is focused on the comparison of the mechanical response of three Ti6Al4V alloys manufactured using different processing methods. Two AM materials were fabricated by means of Selective Laser Sintering (SLS) and Selective Laser Melting (SLM) technologies and employing the processing cycle, including process parameters and post-processing heat treatment, as recommended by the manufacturers.

SLS samples were manufactured using an EOS Titanium Ti6Al4V powder with an EOSINT M 280 (EOS GmbH, Krailling, Germany) powder bed AM machine based on the Direct Metal Laser Sintering (DLMS) technique. The laser power was 260 W with a diameter of 0.1 mm $\pm$ 0.02 mm, and the scan speed was 1200 mm s^{-1}. The hatch spacing, i.e., the distance between two parallel neighboring scanning paths, was 0.1 mm, and the thickness of each layer was 30 µm. The AM process was performed in a controlled argon atmosphere to avoid metal oxidation, and, at the end of the process, samples were heat-treated inside the machine at 650 °C for 180 min in an inert argon atmosphere, followed by furnace cooling.

SLM samples were produced by employing an EOS M 290 apparatus by EOS GmbH (Krailling, Germany), which mounts one IGP Fiber Laser with a maximum power of 400 W. Material powders were provided by TLS Technik GmbH (Niedernberg, Germany). The main processing parameters were a layer thickness of 60 µm, hatch spacing of 0.12 mm, a laser power of 340 W, and a base temperature of 180 °C. The laser travels upon the powder bed at a scanning speed of 1250 mm s^{-1}. Similarly to the SLS material, the manufacturing process was carried out in an inert argon atmosphere, and samples were heat-treated after building for stress relief. Samples were heated to 740 °C, at a heating rate of 7 °C/min, and held at that temperature for 130 min after manufacturing.

Wrought Ti6Al4V grade 5 was supplied as bars (150 mm in length and 12 mm in diameter) and then heat-treated to achieve a martensitic microstructure. The heat-treatment cycle involved holding the material at 1050 °C [6], above the β-transus temperature, for 90 min, followed by water quenching. The material was also subjected to a stress-relief process at 650 °C (heating rate 3 °C/min) for 180 min.

2.2. Specimens

Cylindrical coupon samples were used for metallographic characterization and hardness testing. Uniaxial and compressive tests have been performed on the RBU-S and AC-S geometries presented in Figure 1. For the evaluation of the uniaxial response in compression of the W-WQ material, a new sample geometry (SC-S, Figure 1) has been employed to limit both the influence of friction between the sample and the cross-head of the testing machine and the contact pressure at the interface to avoid steel plates wear during the test.

W-WQ samples were extracted with their axis aligned to the bar's axis. AM samples were manufactured as cylindrical rods and machined to the final geometry. Different orientations for the AM materials were selected to assess the presence of any process-induced anisotropy. For the SLS material, five different orientations were investigated with respect to the building direction (Z) as illustrated in Figure 2a, while for the SLM material, only three building directions were considered, as shown in Figure 2b. Following the manufacturer's instructions for the latter material, alternating the deposition direction between consecutive layers ensures isotropy of the material in the XY plane. Anisotropy is a common feature in several AM alloys [36–40]. However, limited differences in response for dissimilar building orientations in Ti6Al4V after heat-treating have been reported [23,41].
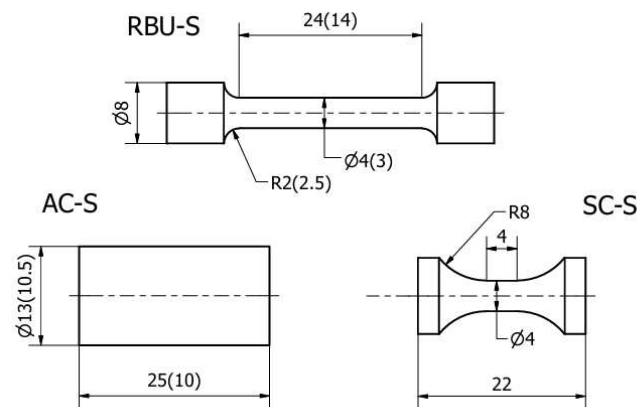

Figure 1. Technical drawing of sample for uniaxial tensile testing (RBU-S) and uniaxial compressive testing (AC-S and SC-S). Dimensions in brackets refer to the SLS samples. Dimensions are in mm.
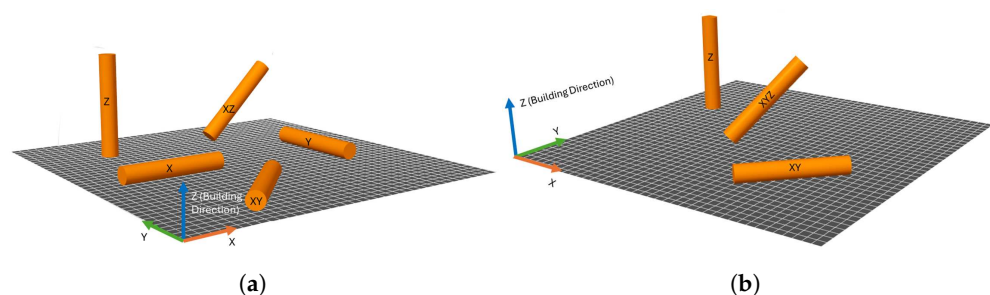

(**a**)   (**b**)

Figure 2. Orientation of the samples in the build chamber and labels (**a**) SLS and (**b**) SLM.

2.3. Experimental Procedures

For microstructure characterization and hardness testing, reference samples were hot-mounted in conductive epoxy resin, ground up to a P4000 SiC paper, then polished with polycrystalline diamond suspensions of 3 μm, 1 μm and 0.25 μm. Materials were then etched using Keller's reagent for 95 s. Microstructural features and phase distribution were investigated using a DM2500M optical microscopy (OM) by Leica Microsystems (Wetzlar, Germany) and Ultra Plus Scanning Electron Microscope (SEM) by Zeiss (Oberkochen, Germany) equipped with a Oxford Instruments (High Wycombe, UK) C-Nano Electron Backscattered Diffraction (EBSD) detector. Fracture surfaces were acquired with a XL30 SEM by Philips (Eindhoven, The Netherlands).

Micro-Vickers Hardness was measured on polished surfaces employing a HX1000 TM by Remet sas (Bologna, Italy). Quasi-static tests were performed with an electromechanical Instron 5586 (Instron Structural Testing, Darmstadt, Germany) with a maximum load capacity of 300 kN, under displacement control, with a constant cross-head velocity selected to achieve nominal strain rates of 5×10^{-4}/s and 1×10^{-2}/s at the beginning of the deformation process (before multiaxiality phenomena such as necking or barreling occurred). High-temperature tests were performed at 5×10^{-4}/s, and samples were heated using an Instron 3019 environmental chamber. Temperature was monitored in the gauge section of the samples using a K-type thermocouple. A clip gauge was employed for room-temperature tensile testing to evaluate gauge section elongation more accurately. For the SLS tensile samples, the reference length of the clip gauge was 12.5 mm, whereas it was set to 22.9 mm for both SLM and W-WQ samples. Table 1 summarizes the experimental tests carried out.

Table 1. Summary of mechanical tests carried out. RT = room temperature; HT = high temperature.

Material and Directions	SLS					SLM			W-WQ
	X	**XY Y**	**XZ**	**Z**		**X**	**XZ**	**Z**	
Uniaxial Tension @ 5×10^{-4}/s and RT	3	3	3	3	3	3	3	3	3
Uniaxial Tension @ 5×10^{-4}/s and HT	4	-	-	-	-	2	-	-	2
Uniaxial Tension @ 1×10^{-2}/s and RT	2	-	-	-	-	2	-	-	2
Uniaxial Compression @ 5×10^{-4}/s and RT	2	-	-	-	2	2	-	2	2

3. Results

3.1. Microstructure

The optical micrographs of the reference samples are shown in Figure 3 for the investigated materials. The layer-wise manufacturing process strongly influences the morphology of the prior-β grain structure of both the SLS and SLM materials. Indeed, the longitudinal sections (Figure 3c–e), parallel to the building direction, exhibit the typical columnar grain structure. The cross-sections, normal to the building direction (Figure 3b–d), are, in contrast, characterized by a more equiaxial, "chess-like", distribution. This morphology is strongly dependent on the manufacturing process and on the local heat-transfer phenomena [18].

An equiaxial grain morphology is also present in the W-WQ material, as visible in Figure 3a. As easily distinguishable in Figure 3, the extremely fast cooling rates in AM processes are responsible for a much finer prior-β structure in both SLS and SLM samples if compared to the W-WQ material. The size of the grain structure is an inverse function of the cooling rate, which, for AM processes, can be as high as 10^5–10^6 °C s^{-1} [13,34], whereas for water quenching, it is approximately 10^3–10^4 °C s^{-1} [4,29]. This difference in cooling rates results in a prior-β grain size of the W-WQ material (computed using the intercept method) that is approximately 40% bigger than the two AM alloys, as reported in Table 2. The presence of α' lamellae within prior-β grains is clearly discernible in optical images as well. A more precise analysis of their distribution was carried out by means of SEM/EBSD investigation.

The as-received Ti6Al4V-grade 5 microstructure is illustrated in Figure 4a. Observing the inverse pole figure (IPF) and the phase map (PM) shows that the typical cellular HCP-α structure is surrounded by intergranular BCC-β phase [17], with the latter measured to be approximately 10%. After the water quenching process, the wrought material presents a fully α' martensitic microstructure, with primary and secondary α' sub-structures [19]. IPF and PM, depicted in Figure 4b, confirm a complete $\beta \rightarrow \alpha'$ transformation.

A similar α' acicular microstructure is also found in both SLS and SLM materials, as illustrated in Figure 4c and Figure 4d, respectively. The concentration of the β phase was measured to be lower than 1% in all martensitic microstructures. The presence of a metastable α' martensite phase in AM Ti6Al4V has been reported in different literature studies [18,34], and it is the result of the extreme thermal gradients developed during material fabrication.
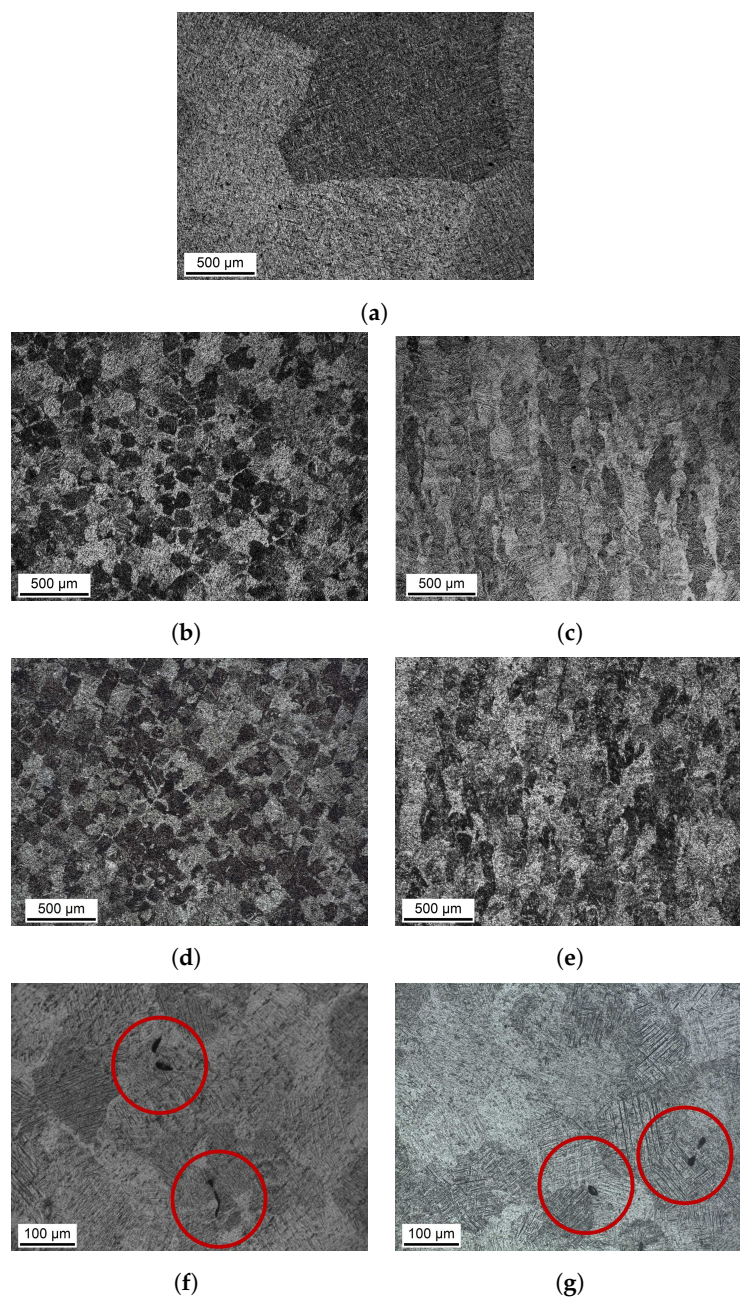
Figure 3. Optical micrographs. (**a**) W-WQ sample. SLS sample—(**b**) cross-section, (**c**) longitudinal section. SLM sample—(**d**) cross-section, (**e**) longitudinal section. Micrographs of AM samples with defects circled in red (**f**) SLS and (**g**) SLM.

Table 2. Average prior-β grain size and lamellae thickness.

Material	Prior-β Average Diameter (μm)	α' Lamellae Thickness (μm)
W-WQ	1150	1.9 ± 0.6
SLS	85	0.9 ± 0.3
SLM	80	1.2 ± 0.4

The size of the lamellar structure, evaluated from the EBSD micrographs, is similar for the two AM materials, whereas they are much larger in the W-WQ alloy. As for the dimensions of the prior-β grains, the thickness of the α' laths is an inverse function of the cooling rate. Compared to the SLS processing method, the slightly larger lamellae observed

in the SLM material may be attributed to the higher temperature employed for the stress-relief process [29]. However, the thermal histories experienced by both materials during manufacturing are extremely complex, and it is not easy to establish a direct correlation.
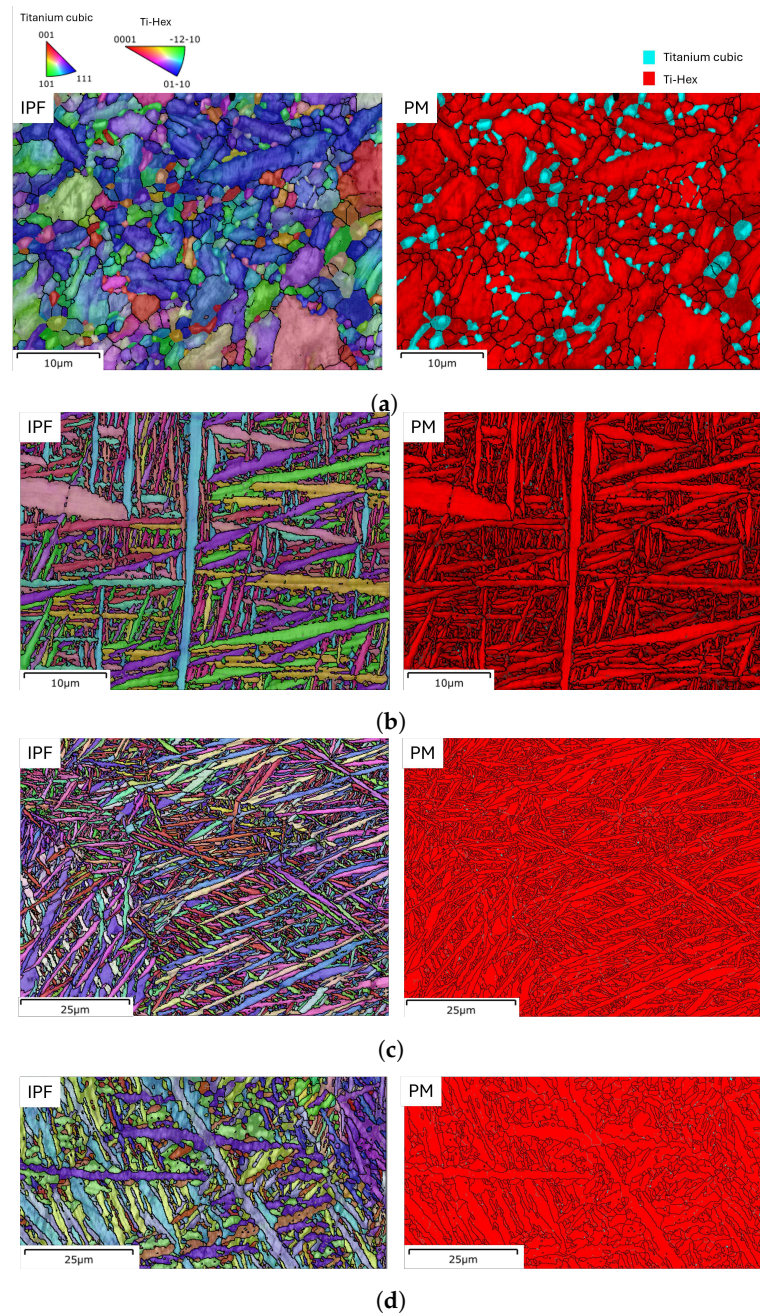

Figure 4. Inverse pole figure (IPF) and phase map (PM) with grain boundaries marked in black of (**a**) as-received wrought material (Ti6Al4V-grade 5), (**b**) W-WQ, (**c**) SLS and (**d**) SLM.

The presence of typical AM porosity defects is also noticeable, and it can be classified into macro- and microporosity [42]. Macroporosity (red circle in Figure 3f,g) is related to LoF (Lack-Of-Fusion) defects, usually irregular in shape, and ~20–60 µm in magnitude. Microporosity, related to gas entrapment during the building process, was also found to be present. However, more detailed microstructural investigations revealed a limited presence of these defects, and both materials exhibited high densification values: the density of the SLS and SLM samples was measured to be approximately 98.6% and 99.5%, respectively, based on a reference value of $4.63\,\mathrm{g\,cm^{-3}}$.

3.2. Mechanical Response

3.2.1. Hardness Testing

The Micro-Vickers Hardness values of the investigated Ti6Al4V alloys are compared in Figure 5. No significant difference between the longitudinal- and cross-sections of the AM materials was observed; thus, an average value is reported. Guzanova et al. [43] reported a reduction in differences in hardness between vertical and horizontal building orientation after stress-relief annealing. All three martensitic microstructures exhibit higher hardness levels than the conventional wrought alloy (green dashed line). These results are associated with a higher concentration of dislocations generated during the phase transformation process [7]. The measured hardness values are instead slightly lower if compared to those reported in [35] for the AB-SLM material, which may be attributed to the partial recovery of process-induced residual stresses in the stress-relieved state. The hardness values of both SLS and SLM samples are closer to the value reported by Al-Rubaie et al. [44] for SR-SLM Ti6Al4V. The lowest hardness was measured in the W-WQ sample microstructure, characterized by larger prior-β grains and α' laths, consistently with the known inverse relationship between hardness and grain size [35,45].
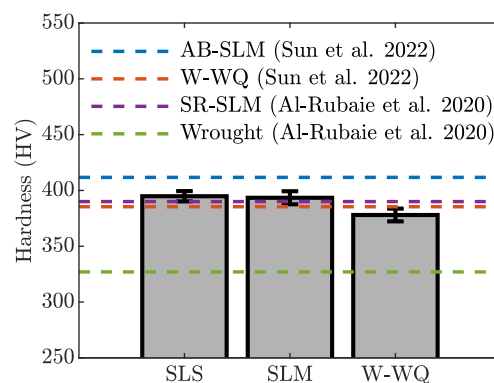

Figure 5. Hardness values for Ti6Al4V samples. Reference data adapted from Refs. [35,44].

3.2.2. Selective Laser Sintering: SLS

Tensile test results conducted on smooth bar specimens (RBU-S) at a strain rate of 5×10^{-4}/s are shown in Figure 6a, for the SLS alloy. Due to the high repeatability of the experimental results, only one curve for direction is displayed. The investigated material manifests similar mechanical responses in the planar directions (X, XY, Y), which lie between the behavior of the Z and XZ samples. The difference among the true stresses at 1% of true plastic strain, σ_1, is limited and varies by approximately 37 MPa (about 3.2% of the average value). In contrast, the values of true stress upon necking, $\sigma_{Necking}$, differ by less than 40 MPa (about 3.5% of the average stress value), as summarized in Table 3. The value of deformation at which plastic instability phenomena occur is slightly higher for the Z and XZ directions than for the samples oriented along the building base.

Figure 6b depicts the influence of deformation rate and temperature on the tensile uniaxial response of the material in the low-rate regime. It is evident that (Table 3):

- Temperature has a strong softening effect on the material yield stress, with a reduction of approximately 18% and 25% in both σ_1 and $\sigma_{Necking}$ at 150 °C and 235 °C, respectively. The shape of the flow curve during the uniform deformation phase is not significantly influenced by temperature. According to Considere's condition, the on-set necking occurs at higher strain levels than those observed in room-temperature testing. Subsequent to necking, the rate of strength reduction is more gradual at elevated temperatures, indicating a dissimilar progression of plastic instability. In addition, thermal softening enhances material deformation and leads to greater Bridgman strain at failure (Table 3).

- The material exhibits a limited, yet present, strain-rate sensitivity in the low-rate regime, with an increase in σ_1 at 1×10^{-2}/s of approximately 3%. By increasing the yield strength, plastic instability occurs for lower strain, along with an increased rate of stress reduction to failure. These results indicate that, under quasi-static conditions, the deformation mechanisms are already thermally activated, even if temperature has a more remarkable influence on material response than the strain rate in this regime [46]. Furthermore, increasing the strain rate results in a higher Bridgman strain at failure compared to lower velocities. This is likely due to the substantial rise in strain rates, by an order of magnitude, in the gauge section during necking, which deviates from isothermal conditions, causing a temperature increase and thus enhancing ductility.

Figure 6b also compares the flow curve under tensile and compressive loading. The strength under the application of negative stress triaxiality is improved by roughly 14% and 18%, if compared to the tensile response, for the X and Z directions, respectively (as reported in Table 3). Tension–compression asymmetry (TCA) has been reported in the literature for commercially pure titanium (CP-Ti) and several Ti-alloys [47–50]. This phenomenon indicates that the mechanisms of plastic deformation are sensitive to the applied stress state, such as the activation of <c + a> dislocations, differences in the critical resolved shear stress for <a> basal slip mechanism, or the polarity of twinning [50–53].
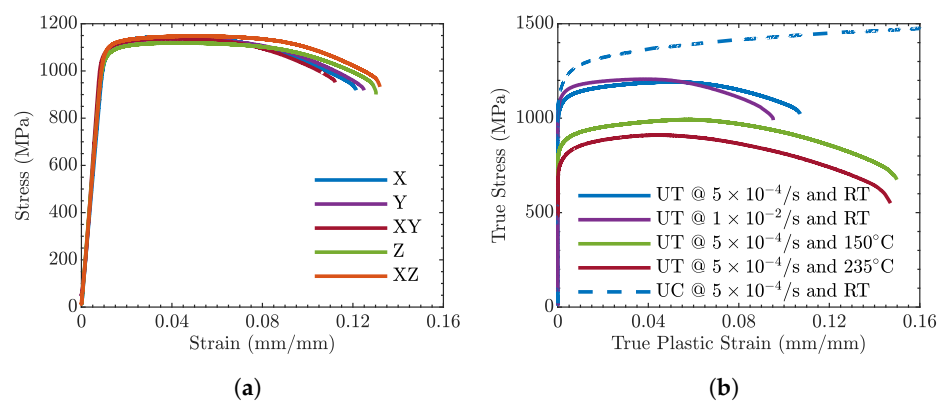

(**a**)   (**b**)

Figure 6. (**a**) Engineering uniaxial tensile curves for the SLS alloy at 5×10^{-4}/s and room temperature. (**b**) Uniaxial tensile (UT) and compressive (UC) true stress vs. true plastic strain curves for different temperatures and strain rates for the SLS alloy for the X direction.

Table 3. Summary of test results for the SLS material. Median values.

Test	Temperature (°C)	Strain-Rate (1/s)	σ_1 (MPa)	$\sigma_{Necking}$ (MPa)	$\varepsilon_{Necking}$ (%)	ε_f^B (%)
RBU-S X	25	5×10^{-4}	1141.1	1179.2	3.2	40.1
RBU-S X	25	1×10^{-2}	1178.1	1195.7	2.0	53.3
RBU-S X	150	5×10^{-4}	926.2	985.6	4.4	94.1
RBU-S X	235	5×10^{-4}	854.6	905.4	3.4	112.3
RBU-S Y	25	5×10^{-4}	1144.1	1179.6	2.9	37.6
RBU-S XY	25	5×10^{-4}	1141.3	1178.0	2.9	40.3
RBU-S Z	25	5×10^{-4}	1115.6	1157.3	3.3	35.1
RBU-S XZ	25	5×10^{-4}	1152.5	1199.0	3.7	41.6
AC-S X	25	5×10^{-4}	1282.8	N.A.	N.A.	N.A.
AC-S Z	25	5×10^{-4}	1308.3	N.A.	N.A.	N.A.

σ_1: True Stress at 1 %; $\sigma_{Necking}$: True stress upon necking; $\varepsilon_{Necking}$: True plastic strain upon necking; ε_f^B: Bridgman deformation at failure.

3.2.3. Selective Laser Melting: SLM

This section presents the results of the mechanical testing campaign carried out on the SLM samples. Engineering uniaxial tensile curves are illustrated in Figure 7a: as

already reported for the SLS material, it is possible to appreciate a slight difference in response among the investigated orientations. The horizontally printed sample (XY) is characterized by a higher strength than the vertically printed one (Z) and the 45° one (XYZ), together with a reduced strain-to-failure value. The differences in the σ_1 and $\sigma_{Necking}$ are 3.1% and 2.1% respectively, and are summarized in Table 4. Nevertheless, anisotropy is negligible between the investigated orientations and is bounded in the experimental scatter, suggesting that directional variances, while existing, do not have an important impact on the overall response of the material. Temperature, strain rate, and the direction of applied loading exert a noticeable impact on material behavior, which is consistent with the results on the SLS alloy. The increase in temperature determines a reduction in true stress at 1% of approximately 12% at 100 °C and a slower evolution of plastic instability phenomena, with an improvement in the deformation at failure of 140%. The influence of temperature contrasts with the effect of the strain rate, as visible in Figure 7b and reported in Table 4. With an increasing strain rate, σ_1 and ε_f^B are, respectively, 1.3% and 51% higher than in the reference configuration, while $\varepsilon_{Necking}$ is decreased by 20.5%. Under compression, referring to σ_1, material resistance increases by approximately 11 % (XY direction) to 18% (Z direction), as summarized in Table 4.
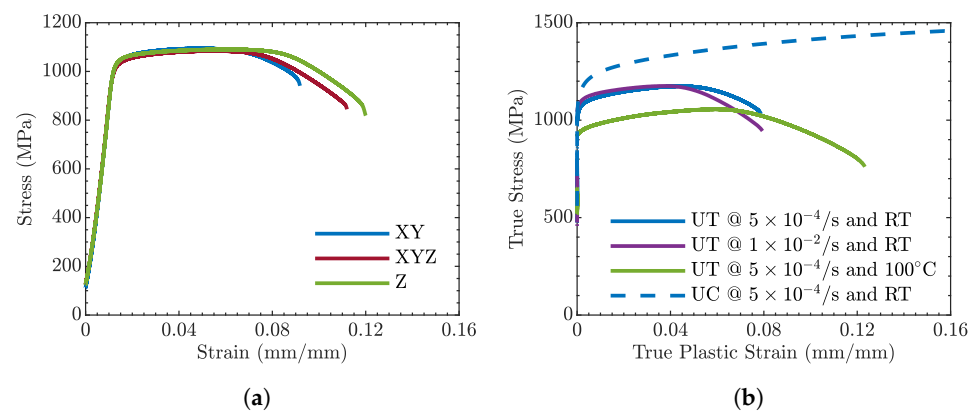

(**a**)   (**b**)

Figure 7. (**a**) Engineerig uniaxial tensile curves for the SLM alloy at 5×10^{-4}/s and room temperature. (**b**) Uniaxial tensile (UT) and compressive (UC) true stress vs. true plastic strain curves for different temperatures and strain rates for the SLM alloy for the XY direction.

Table 4. Summary of test results for the SLM material.

Test	Temperature (°C)	Strain-Rate (1/s)	σ_1 (MPa)	$\sigma_{Necking}$ (MPa)	$\varepsilon_{Necking}$ (%)	ε_f^B (%)
RBU-S XY	25	5×10^{-4}	1121.5	1168.9	3.4	36.7
RBU-S XY	25	1×10^{-2}	1139.6	1169.7	2.7	55.5
RBU-S XY	100	5×10^{-4}	979.6	1050.2	4.5	88.1
RBU-S Z	25	5×10^{-4}	1094.9	1153.7	4.5	61.6
RBU-S XYZ	25	5×10^{-4}	1087.2	1144.3	4.1	58.3
AC-S XY	25	5×10^{-4}	1237.4	N.A.	N.A.	N.A.
AC-S Z	25	5×10^{-4}	1294.9	N.A.	N.A.	N.A.

σ_1: True Stress at 1 %; $\sigma_{Necking}$: True stress upon necking; $\varepsilon_{Necking}$: True plastic strain upon necking; ε_f^B: Bridgman deformation at failure.

3.2.4. Wrought-Water Quenched: W-WQ

The uniaxial tensile behavior of W-WQ material is displayed in Figure 8. It is evident that raising the temperature or lowering the strain rate reduces the yield stress and increases the failure strain. Indeed, σ_1 decreases from 1073.7 MPa at room temperature to 786.6 MPa at 150 °C, whereas the Bridgman deformation at failure improves from 6.1% to 17.8%. The lack of an extensive post-necking regime at room temperature suggests that the material reaches its fracture point very quickly after reaching the maximum engineering stress. This is in contrast with the behavior exhibited by both AM alloys, characterized by a remarkable

post-necking regime, which was accompanied by the accumulation of significant plastic deformation prior to failure. The influence of the strain rate on the material response is more pronounced in the W-WQ alloy. In fact, at 1% of strain, the true stress response increases by 6.8%. Tension–compression asymmetry, as visible in Figure 8, is approximately of 8.5%.
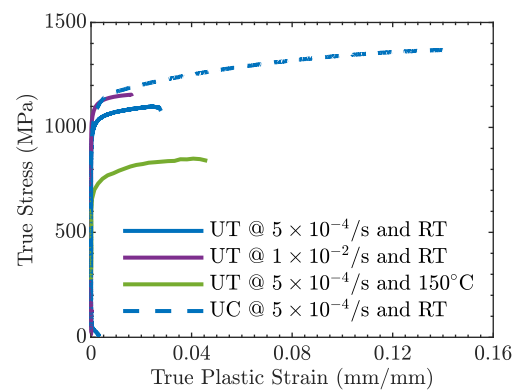

Figure 8. Uniaxial tensile (UT) and compressive (UC) true stress vs. true plastic strain curves for different temperatures and strain rates for the W-WQ alloy.

4. Discussion

4.1. AM of Ti6Al4V

Anisotropy, due to the layerwise deposition technique, is a typical feature of AM materials. It can be attributed to the directionality of the grain morphology, with grains elongated along the building direction [16,54] (also reported in Figure 3), and to different distributions of residual stresses (and thus dislocation density) resulting from the manufacturing processes [26,54]. The volume subjected to repeated thermal cycles varies with the building orientation, leading to distinct local temperature history evolution and cooling rates [26,55]. This causes anisotropy to be more relevant in AM Ti6Al4V in the as-built state [23,26,41]. Table 5 presents the yield stress (YS) and ultimate tensile stress (UTS) values measured for AM Ti6Al4V alloys, as reported in various literature sources and investigated in this study, to assess the effects of different deposition technologies and post-processing treatments. Both Cain et al. [41] and Simonelli et al. [23] investigated the response of SLM Ti6Al4V in the as-built state and after various stress-relief treatments. Their analyses indicate that the anisotropy between horizontally and vertically printed samples diminishes as the post-processing stress-relief temperature increases, together with a reduction in material strength, as reported by [16,24] as well. In Cain's investigation, anisotropy in the yield stress decreased from 3% in the as-built state to less than 1% after heat-treating at 890 °C. Vilaro et al. [16] observed a reduction in anisotropy in yield strength with post-processing treatments as well, which declined from 15% in the as-built condition to 6% after heat-treating at 730 °C and to less than 1% after heat-treating at 980 °C. By increasing the post-processing temperature, microstructural evolution phenomena, such as the growth of the α' laths thickness, is promoted [29], which might favor the reduction in the material strength. Several authors also reported the decomposition of the martensitic microstructure, starting from approximately 800 °C, into an $\alpha + \beta$ structure [26,27,56,57]. For instance, Lee et al. [26] documented the formation of the typical Widmanstätten microstructure, together with changes in the mechanical response, after heat-treating AM martensitic samples at 850 °C. Similarly, Bai et al. [24] found an $\alpha + \beta$ microstructure after all heat treatments involving a soaking temperature of at least 850 °C, and, by increasing the post-processing temperature, both YS and UTS were reduced. From the comparison, the SLS and SLM materials investigated in this study exhibited responses comparable to those reported in the literature. The mechanical behavior of the SLS alloy in the X-Y plane demonstrates no significant anisotropy, indicating uniform material properties for these orientations. Similarly, in the X-Z plane, anisotropy is present yet negligible, with

differences in yield and ultimate tensile stresses being less than 4% and 2.5%, respectively. The analysis of the SLM is also in line with what was stated for SLS. In this case, differences in yield and ultimate tensile stresses are less than 1.5% and 2.5%, respectively, between the horizontally and vertically printed samples. The consistency between the SLS and SLM materials indicates that both additive manufacturing techniques can produce titanium alloys with similar mechanical performances. Furthermore, post-processing heat treatment effectively minimizes directional dependence on mechanical behavior.

Table 5. Comparison of the yield stress (YS) and ultimate tensile stress (UTS) for AM Ti6Al4V for different manufacturing techniques.

Author	AM Process	Heat Treatment	Microstructure	Direction/ Position	YS (MPa)	UTS (MPa)
Cain et al. [41]	SLM	AB	α'	X/flat Z	1093 1125	1279 1216
		650 °C-4 h + FC	α'	X/flat Z	1145 1132	1187 1156
		890 °C-2 h + FC	$\alpha+\beta$	X/flat Z	973 964	996 998
Simonelli et al. [23]	SLM	AB	α'	X/flat X/edge Z	1075 978 967	1199 1143 1117
		730 °C-4 h + FC	$\alpha + \beta$	X/flat X/edge Z	974 958 937	1065 1057 1052
Vilaro et al. [16]	SLM	AB	α'	X Y	1137 962	1206 1166
		1050 °C-1 h + WQ	α'	X Y	913 836	1019 951
		980 °C-1 h + WQ	$\alpha + \beta + \alpha'$	X Y	944 925	1036 1040
		730 °C-2 h + AC	$\alpha + \beta + \alpha'$	X Y	965 900	1046 1000
Amsterdam and Kool [56]	LBD	970 °C-1 h + WQ	$\alpha+\beta$	X Z	973 943	1073 1073
		538 °C + AC	$\alpha+\beta$	X Z	1063 1045	1162 1141
Wang et al. [58]	DMLM	800 °C-2 h + FC	$\alpha + \beta$	X Z	988 982	1053 1037
Carroll et al. [59]	DED	AB	N.A.	X/edge Z	960 945	1063 1041
Sun et al. [60]	SLM	750–850 °C-5 h	N.A.	X XZ Z	858 883 888	936 964 953
Bai et al. [24]	SLM	AB	α'	N.A.	1065	1152
		850 °C-2 h + FC	$\alpha + \beta$	N.A.	943	989
		950 °C-2 h + FC	$\alpha + \beta$	N.A.	835	887
		1020 °C-2h + FC	$\alpha + \beta$	N.A.	742	839
		CA	Bimodal	N.A.	1054	1196
Lee et al. [26]	SLM (Ti64ELI)	AB	α'	X Z	1372 1278	1656 1602
		800 °C-2 h + AC	$\alpha + \beta$	X Z	1101 1029	1615 1537
		900 °C-2 h + AC	$\alpha + \beta + \alpha'$	X Z	1007 969	1501 1837
		950 °C-2 h + AC	$\alpha + \beta + \alpha'$	X Z	1017 939	1689 1609
This work	SLS	635 °C-3 h + FC	α'	X Y XY Z XZ	1067.2 1081.9 1082.2 1057.3 1101.6	1141.2 1143.7 1144.8 1124.9 1153.6
	SLM	740 °C-2 h + FC	α'	XY XYZ Z	1052.5 1027.7 1051.9	1114.8 1087.6 1096.4

4.2. Comparison of Wrought and AM Ti6Al4V

All investigated materials do not show a significant difference between the yield and maximum stress, characteristic of the Ti6Al4V martensitic microstructure [35,61]. The comparison of the true stress vs. true plastic strain response until necking is reported in Figure 9a. The plastic behavior of all three alloys is described well by the same Hockett–Sherby [62] work-hardening law, in which only the reference yield stress value σ_0 changes for the different alloys. The two AM materials demonstrate similar yield and ultimate tensile stresses, both of which are higher than those observed in the W-WQ material. These differences can be primarily attributed to the varying sizes of the prior-β grains and α' laths thickness among the investigated materials, as summarized in Table 2. Chong et al. [61] examined the behavior of martensitic Ti6Al4V for different prior-β grain sizes and concluded that prior-β grain refinement, which is also associated with a reduced thickness of the α' laths, contributes significantly to the strengthening of the material. Both Cao et al. [63] and Sun et al. [35] showed that the yield strength of α'-martensitic Ti6Al4V is governed by the lamellae thickness according to a Hall–Patch relationship. Indeed, smaller α' lamellae promote more significant dislocation pile-up phenomena at their boundaries, resulting in higher yield strength and ultimate tensile stress value [17]. Figure 9b compares the hardening response of the three Ti6Al4V alloys investigated in this study with the data reported in [10,35]. Sun et al. [35] addressed the responses of SLM and W-WQ Ti6Al4V in the as-built conditions, which exhibit similar behavior to the AM martensitic microstructures investigated in this study, with very high values of yield and maximum stresses. The material investigated by Chen et al. [10], a commercial-grade Ti6Al4V with a lamellar $\alpha + \beta$ microstructure, exhibits a lower yield strength, together with an increased hardening rate and ductility. The properties of $\alpha + \beta$ alloys are usually bounded between those of the α phase, characterized by a higher strength and lower ductility [10], and of the β phase, which exhibits the opposite behavior [5,64].

High similarities can be found in the temperature-softening response below 500 °C of wrought and AM Ti6Al4V, as depicted in Figure 9c. Data for wrought Ti6Al4V were sourced from Chen et al. [10], while data for Ti6Al4V fabricated using Direct Laser Deposition (DLD) were taken from Ivanov et al. [65]. Regardless of the manufacturing technique and final microstructure, there is a consistent thermal softening trend. This may be attributed to the fact that the hexagonal close-packed (HCP) metals exhibit a constitutive behavior that is intermediate between body-centered cubic (BCC) and face-centered cubic (FCC) metals [66,67]. Depending on their specific microstructure and composition, the thermal response of HCP metals can align more closely with either BCC or FCC structures [54]. Lennon and Ramesh [66] showed that BCC vanadium and HCP α titanium manifested similar high-temperature sensitivity. Therefore, the presence of BCC-β phase in the wrought Ti6Al4V investigated in [10] might not significantly alter its high-temperature response.

The Bridgman deformation at fracture was observed to increase from 6.1% in the W-WQ alloy to slightly lower than 40% in the AM materials, which demonstrated a notable post-necking deformation. This result indicates that the behavior of the wrought material is significantly less ductile. To probe the role of microstructure on ductility, fracture surfaces of uniaxial tensile samples, tested at a strain rate of 5×10^{-4}/s and at room temperature, were further investigated. For the AM materials, horizontally printed samples were taken into consideration.

The overview of the fracture surface for the W-WQ material (Figure 10a) illustrates a cleavage fracture surface development, with a staircase morphology (Figure 11a,b) and a mixed ductile transgranular fracture together with cleavage facets [34]. Both SLS (Figure 10b) and SLM (Figure 10c) samples present the typical cup-con fracture surface: a fracture initiates by void formation at the center of the sample, where the highest localization of deformation occurs during necking and propagates through the minimum cross-section [68]. Near the borders—where axisymmetric effects are less pronounced—failure is led by rapid shear tearing. In martensitic Ti6Al4V, cracks are found to form and propagate along α' lamellae boundaries [61,69]. Sun et al. [35] reported that the formation of

voids within α' laths was followed by shear-stress-driven coalescence that results in the nucleation of ductile dimples. Propagation then occurs by cleavage within martensite variants and their interfaces [7]. The lower ductility of W-WQ alloy compared to AM alloys can be attributed to the dimension of the α' lamellae. Refining the α' phase increases the possibility of cracks being arrested when they encounter lamellae with different orientations [61]. Furthermore, the high-angle boundaries between α' laths promote a mixed intra-prior-β and intra-α' fracture mode [35,54]. This causes a quasi-cleavage fracture (with a terrace-like morphology) along prior-β boundaries that is clearly visible in Figure 11c,e for the SLS and SLM alloys, respectively, and in Figure 11b for the W-WQ alloy. Indeed, Simonelli et al. [23] related the terrace-like morphology in SLM Ti6Al4V to the crack propagation mechanism through the prior-β grains along α' laths boundaries. Furthermore, Chong et al. [61] reported that the average crack length decreases with an increase in the size of the prior-β grains, which serve to deflect and eventually arrest crack propagation [35]. Thus, the refinement of prior-β grains is another factor contributing to the higher ductility observed in AM alloys. The presence of pores and process-induced defects was recorded in both SLS and SLM alloys (indicated with a red arrow in Figure 11d,f). However, no clear evidence suggests their contribution as damage nucleation sites, as also reported in [23,54].
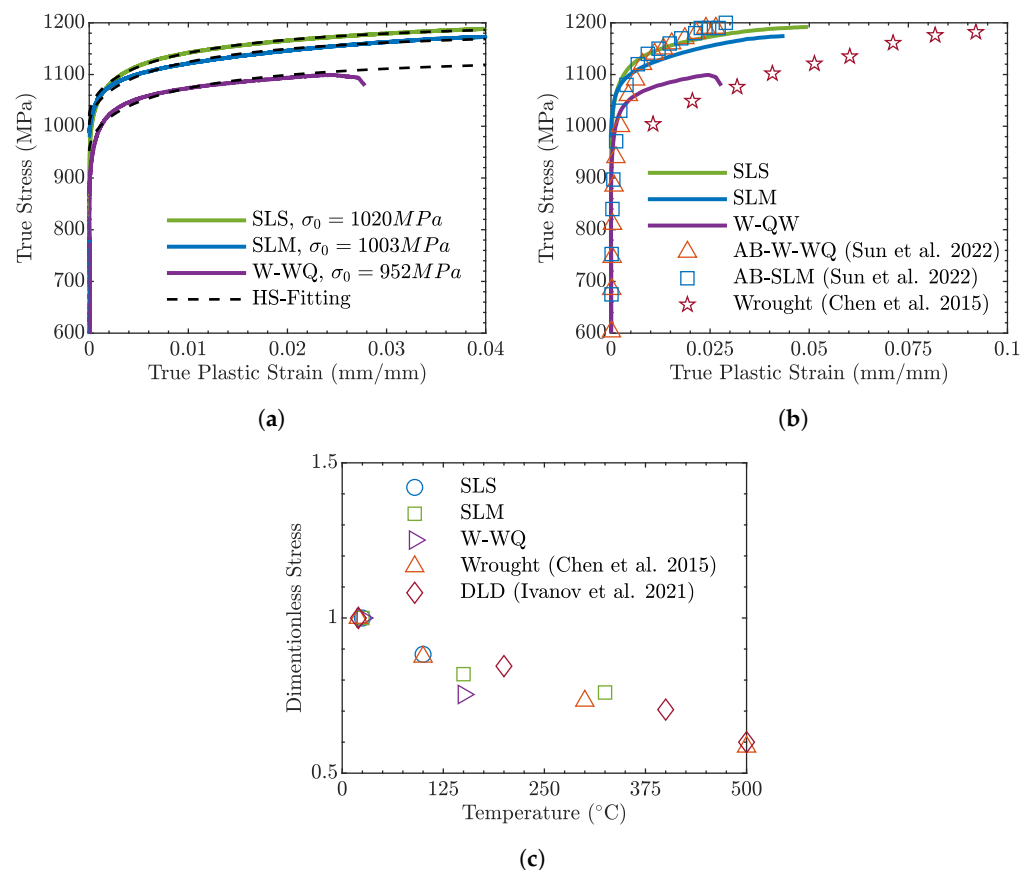

Figure 9. (**a**) Comparison of the flow curve at $5 \times 10^{-4}/\text{s}$ and RT for the SLS (X), SLM (XY), and W-WQ materials. Fitting with an H–S expression: $\sigma_y = \sigma_0 + 180.1(1 - exp(-\varepsilon_p^{0.58}))$. (**b**) Comparison of the flow curve of AM and Wrought Ti6Al4V. Adapted from Refs. [10,35]. (**c**) Comparison of the influence of temperature on the response of AM and Wrought Ti6Al4V up to 500 °C for $\varepsilon_p = 0.02$. DLD data are for $\varepsilon_p = 0.002$. Literature data are adapted from Refs. [10,65].
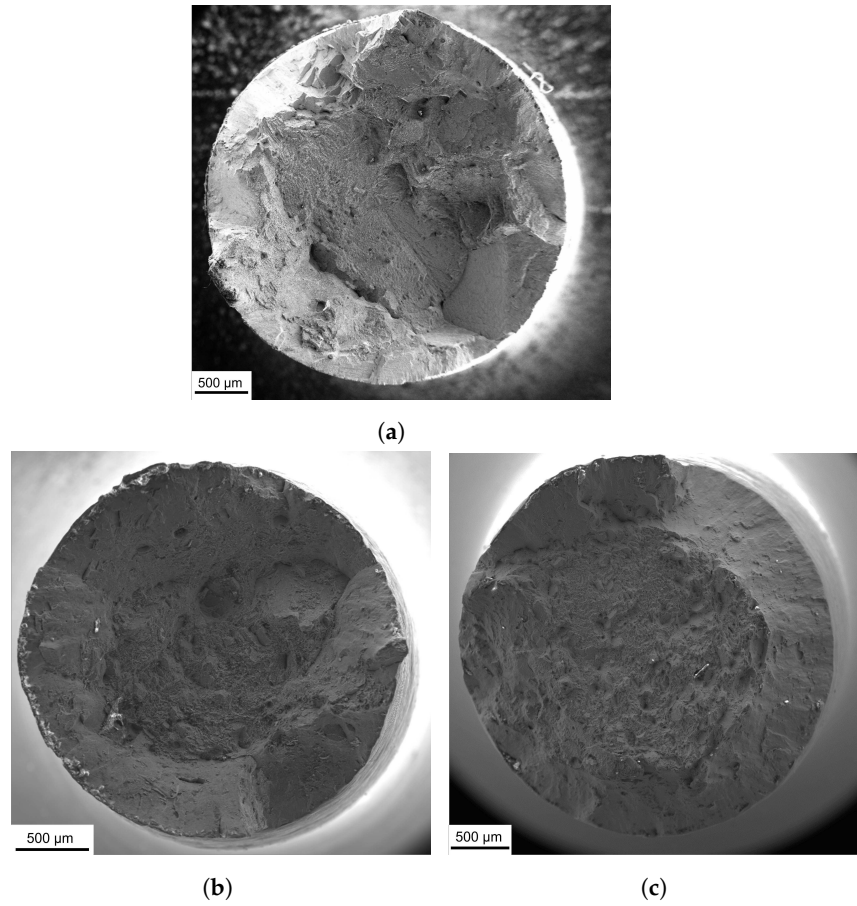
(**a**)

(**b**)

(**c**)

Figure 10. Overview of UT fracture surfaces: (**a**) W-WQ; (**b**) SLS; (**c**) SLM.

(**a**)

(**b**)

(**c**)

(**d**)

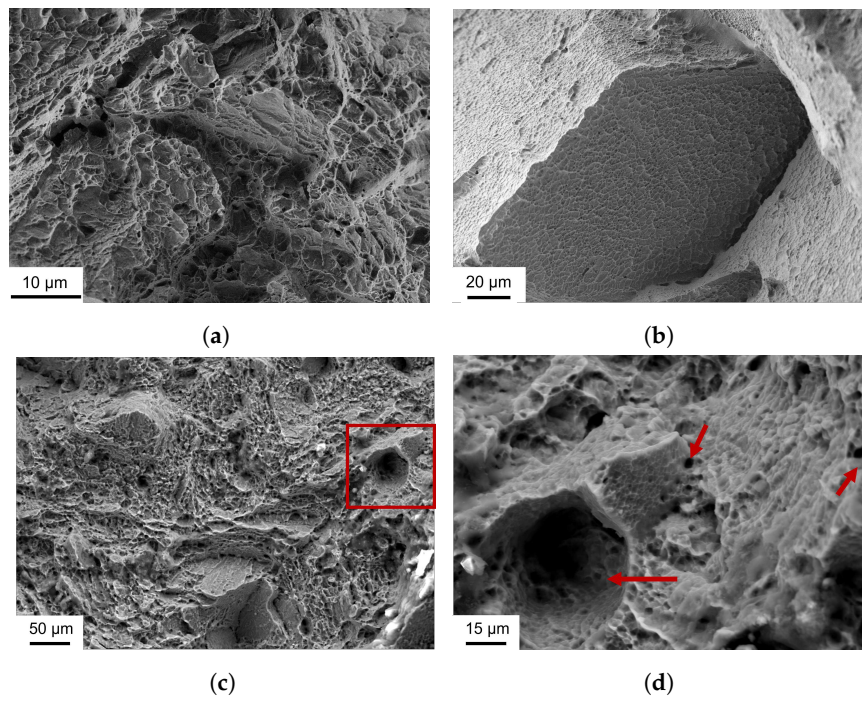**Figure 11.** *Cont.*

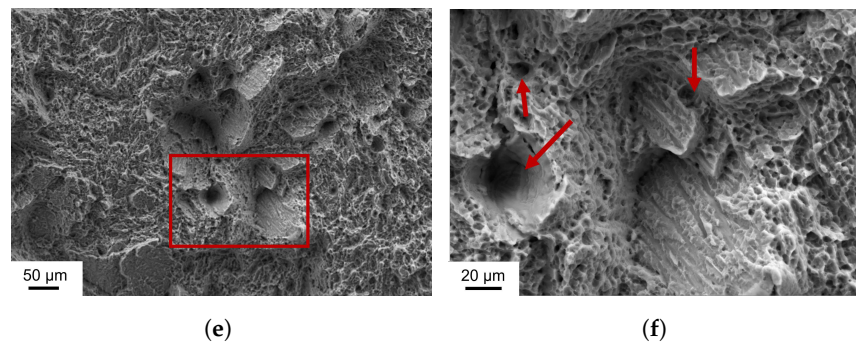|	
(**e**)	(**f**)

Figure 11. Fractographic analysis on UT samples. W-WQ: (**a**) Transgranular fracture; (**b**) cleavage facets. SLS: (**c**) transgranular fracture and terrace-like morphology; (**d**) process-induced defects and dimples. SLM: (**e**) transgranular fracture and terrace-like morphology; (**f**) process-induced defects and dimples. Red boxes indicate the areas investigated at higher magnifications. AM defects and porosity are marked by red arrows.

5. Conclusions

Microstructure and processing play a pivotal role in determining the behavior of Ti6Al4V. In this work, the response of three martensitic Ti6Al4V alloys, manufactured by Selective Laser Sintering, Selective Laser Melting, and water-quenching of a commercial grade, has been investigated. All materials were subjected to a stress-relief treatment before mechanical characterization. Additionally, microstructural and fractographic analyses were performed to examine grain structure, phase composition, and failure mechanisms. The main conclusions that can be drawn are as follows.

- Additive manufacturing enables the fabrication of a very fine martensitic microstructure, characterized by the distribution of needle-like α' phase within the prior-β structure.
- No significant anisotropic behavior was identified along different building orientations under tension for the SLS and SLM materials. This indicates that directional differences are negligible in the stress-relieved state.
- A similar work hardening response under tension was identified in all investigated materials. Differences in yield stress and ductility can be attributed to the dissimilar thicknesses of α' laths and prior-β grains, which strongly influence material deformation and fracture. Compared to the commercial grade Ti6Al4V, the martensitic microstructures exhibit higher hardness and strength. The finer α' laths present in AM alloys contribute to minimizing the significant reduction in ductility observed in W-WQ titanium alloys, especially when compared to wrought Ti6Al4V.
- Tension–compression asymmetry, which indicates that the deformation mechanisms are sensitive to the sign of the applied load, was observed in all three materials. For SLS and SLM Ti6Al4V, asymmetry was found to be higher in the vertically printed samples.
- Strength reduction at high temperatures follows the same trend as conventional Ti6Al4V, suggesting that thermal softening is more influenced by the crystallographic lattice than microstructural features.

The response of AM martensitic Ti6Al4V shows characteristics akin to those of the wrought water-quenched material. However, additive processes result in finer microstructures, which lead to improved performance with both higher strength and enhanced ductility compared to the conventional water-quenched counterpart.

Author Contributions: Conceptualization, G.I.; methodology, G.I. and S.R.; software, S.R.; validation, G.I.; formal analysis, S.R. and G.I.; investigation, G.I. and S.R.; resources, G.I.; data curation, S.R.; writing—original draft preparation, S.R.; writing—review and editing, G.I.; visualization, G.I. and S.R.; supervision, G.I.; project administration, G.I.; funding acquisition, G.I. All authors have read and agreed to the published version of the manuscript.

text of the "MBDA Innovation Award for innovative R&D activity in the field of enabling technology for missile applications".

References

1. Özsoy, K.; Duman, B.; Gültekin, D. Metal Part Production with Additive Manufacturing for Aerospace and Defense Industry Metal Part Production with Additive Manufacturing for Aerospace and Defense Industry Havac ı l ı k ve Savunma Sanayisi İ çin Eklemeli İ malatla Metal Parça Üretimi. *Int. J. Technol. Sci.* **2020**, *11*, 201–211.
2. Kumar, R.; Kumar, M.; Chohan, J.S. The role of additive manufacturing for biomedical applications: A critical review. *J. Manuf. Process.* **2021**, *64*, 828–850. [CrossRef]
3. Liu, S.; Shin, Y.C. Additive manufacturing of Ti6Al4V alloy: A review. *Mater. Des.* **2019**, *164*, 107552. [CrossRef]
4. Lütjering, G. Influence of processing on microstructure and mechanical properties of ($\alpha + \beta$) titanium alloys. *Mater. Sci. Eng. A* **1998**, *243*, 32–45. [CrossRef]
5. Morita, T.; Hatsuoka, K.; Iizuka, T.; Kawasaki, K. Strengthening of Ti-6Al-4V alloy by short-time duplex heat treatment. *Mater. Trans.* **2005**, *46*, 1681–1686. [CrossRef]
6. Pinke, P.; Caplovic, L.; Kovacs, T. The influence of heat treatment on the microstructure of the casted ti6al4v titanium alloy. *Slovak Univ. Technol. Bratislava* **2011**, *11*.
7. Matsumoto, H.; Yoneda, H.; Sato, K.; Kurosu, S.; Maire, E.; Fabregue, D.; Konno, T.J.; Chiba, A. Room-temperature ductility of Ti-6Al-4V alloy with α' martensite microstructure. *Mater. Sci. Eng. A* **2011**, *528*, 1512–1520. [CrossRef]
8. Markovsky, P.E.; Semiatin, S.L. Tailoring of microstructure and mechanical properties of Ti-6Al-4V with local rapid (induction) heat treatment. *Mater. Sci. Eng. A* **2011**, *528*, 3079–3089. [CrossRef]
9. Semiatin, S.; Knisley, S.; Fagin, P.; Zhang, F.; Barker, D. Microstructure Evolution during Alpha-Beta Heat Treatment of Ti-6Al-4V. *Metall. Mater. Trans. A* **2003**, *34A*, 2003–2377. [CrossRef]
10. Chen, G.; Ren, C.; Qin, X.; Li, J. Temperature dependent work hardening in Ti-6Al-4V alloy over large temperature and strain rate ranges: Experiments and constitutive modeling. *Mater. Des.* **2015**, *83*, 598–610. [CrossRef]
11. Bartolomeu, F.; Buciumeanu, M.; Pinto, E.; Alves, N.; Silva, F.S.; Carvalho, O.; Miranda, G. Wear behavior of Ti6Al4V biomedical alloys processed by selective laser melting, hot pressing and conventional casting. *Trans. Nonferrous Met. Soc. China* **2017**, *27*, 829–838. [CrossRef]
12. Irwin, J.; Reutzel, E.W.; Michaleris, P.; Keist, J.; Nassar, A.R. Predicting Microstructure from Thermal History during Additive Manufacturing for Ti-6Al-4V. *J. Manuf. Sci. Eng. Trans. ASME* **2016**, *138*, 1–11. [CrossRef]
13. Masoomi, M.; Thompson, S.M.; Shamsaei, N. Laser powder bed fusion of Ti-6Al-4V parts: Thermal modeling and mechanical implications. *Int. J. Mach. Tools Manuf.* **2017**, *118–119*, 73–90. [CrossRef]
14. He, K.; Zhao, X. 3D thermal finite element analysis of the SLM 316L parts with microstructural correlations. *Complexity* **2018**, *2018*, 6910187. [CrossRef]
15. Ricci, S.; Testa, G.; Iannitti, G.; Ruggiero, A. Laser powder bed fusion of AlSi10Mg alloy: Numerical investigation on the temperature field evolution. *Forces Mech.* **2022**, *8*, 100109. [CrossRef]
16. Vilaro, T.; Colin, C.; Bartout, J.D. As-fabricated and heat-treated microstructures of the Ti-6Al-4V alloy processed by selective laser melting. *Metall. Mater. Trans. A Phys. Metall. Mater. Sci.* **2011**, *42*, 3190–3199. [CrossRef]
17. Shunmugavel, M.; Polishetty, A.; Littlefair, G. Microstructure and Mechanical Properties of Wrought and Additive Manufactured Ti-6Al-4V Cylindrical Bars. *Procedia Technol.* **2015**, *20*, 231–236. [CrossRef]
18. Thijs, L.; Verhaeghe, F.; Craeghs, T.; Humbeeck, J.V.; Kruth, J.P. A study of the microstructural evolution during selective laser melting of Ti-6Al-4V. *Acta Mater.* **2010**, *58*, 3303–3312. [CrossRef]
19. Yang, J.; Yu, H.; Yin, J.; Gao, M.; Wang, Z.; Zeng, X. Formation and control of martensite in Ti-6Al-4V alloy produced by selective laser melting. *Mater. Des.* **2016**, *108*, 308–318. [CrossRef]
20. Bordin, A.; Bruschi, S.; Ghiotti, A.; Bucciotti, F.; Facchini, L. Comparison between wrought and EBM Ti6Al4V machinability characteristics. *Key Eng. Mater.* **2014**, *611–612*, 1186–1193. [CrossRef]
21. Beyl, K.; Mutombo, K.; Kloppers, C.P. Tensile properties and microstructural characterization of additive manufactured, investment cast and wrought Ti6Al4V alloy. *IOP Conf. Ser. Mater. Sci. Eng.* **2019**, *655*, 012023. [CrossRef]

22. Ren, X.P.; Li, H.Q.; Guo, H.; Shen, F.L.; Qin, C.X.; Zhao, E.T.; Fang, X.Y. A comparative study on mechanical properties of Ti-6Al-4V alloy processed by additive manufacturing vs. traditional processing. *Mater. Sci. Eng. A* **2021**, *817*, 141384. [CrossRef]

23. Simonelli, M.; Tse, Y.Y.; Tuck, C. Effect of the build orientation on the mechanical properties and fracture modes of SLM Ti-6Al-4V. *Mater. Sci. Eng. A* **2014**, *616*, 1–11. [CrossRef]

24. Bai, H.; Deng, H.; Chen, L.; Xianbo, L.; Qin, L.; Zhang, D.; Liu, T.; Cui, X. Effect of Heat Treatment on the Microstructure and Mechanical Properties of Selective Laser-Melted Ti64 and Ti-5Al-5Mo-5V-1Cr-1Fe. *Metals* **2021**, *11*, 534. [CrossRef]

25. Mierzejewska, Z.A. Effect of laser energy density, internal porosity and heat treatment on mechanical behavior of biomedical TI6AL4V alloy obtained with DMLS technology. *Materials* **2019**, *12*, 2928. [CrossRef]

26. Lee, J.R.; Lee, M.S.; Yeon, S.M.; Kang, D.; Jun, T.S. Influence of heat treatment and loading direction on compressive deformation behaviour of Ti–6Al–4V ELI fabricated by powder bed fusion additive manufacturing. *Mater. Sci. Eng. A* **2022**, *831*, 142258. [CrossRef]

27. Wang, D.; Wang, H.; Chen, X.; Liu, Y.; Lu, D.; Liu, X.; Han, C. Densification, Tailored Microstructure, and Mechanical Properties of Selective Laser Melted Ti–6Al–4V Alloy via Annealing Heat Treatment. *Micromachines* **2022**, *13*, 331. [CrossRef]

28. Waqas, M.; He, D.; Liu, Y.; Riaz, S.; Afzal, F. Effect of Heat Treatment on Microstructure and Mechanical Properties of Ti6Al4V Alloy Fabricated by Selective Laser Melting. *J. Mater. Eng. Perform.* **2023**, *32*, 680–694. [CrossRef]

29. Lu, S.L.; Zhang, Z.J.; Liu, R.; Qu, Z.; Wang, B.; Zhou, X.H.; Eckert, J.; Zhang, Z.F. Prior β grain evolution and phase transformation of selective laser melted Ti6Al4V alloy during heat treatment. *J. Alloys Compd.* **2022**, *914*, 165235. [CrossRef]

30. Lu, S.L.; Zhang, Z.J.; Liu, R.; Qu, Z.; Li, S.J.; Zhou, X.H.; Duan, Q.Q.; Zhang, B.N.; Zhao, X.M.; Zhao, W.; et al. Tailoring hierarchical microstructures to improve the strength and plasticity of a laser powder bed fusion additively manufactured Ti-6Al-4V alloy. *Addit. Manuf.* **2023**, *71*, 103603. [CrossRef]

31. Vrancken, B.; Thijs, L.; Kruth, J.P.; Van Humbeeck, J. Heat treatment of Ti6Al4V produced by Selective Laser Melting: Microstructure and mechanical properties. *J. Alloys Compd.* **2012**, *541*, 177–185. [CrossRef]

32. Ganor, Y.I.; Tiferet, E.; Vogel, S.C.; Brown, D.W.; Chonin, M.; Pesach, A.; Hajaj, A.; Garkun, A.; Samuha, S.; Shneck, R.Z.; et al. Tailoring microstructure and mechanical properties of additively-manufactured ti6al4v using post processing. *Materials* **2021**, *14*, 658. [CrossRef] [PubMed]

33. Zafari, A.; Barati, M.R.; Xia, K. Controlling martensitic decomposition during selective laser melting to achieve best ductility in high strength Ti-6Al-4V. *Mater. Sci. Eng. A* **2019**, *744*, 445–455. [CrossRef]

34. Xu, Y.; Zhang, D.; Guo, Y.; Hu, S.; Wu, X.; Jiang, Y. Microstructural tailoring of As-Selective Laser Melted Ti6Al4V alloy for high mechanical properties. *J. Alloys Compd.* **2020**, *816*, 152536. [CrossRef]

35. Sun, S.; Zhang, D.; Palanisamy, S.; Liu, Q.; Dargusch, M.S. Mechanical properties and deformation mechanisms of martensitic Ti6Al4V alloy processed by laser powder bed fusion and water quenching. *Mater. Sci. Eng. A* **2022**, *839*, 142817. [CrossRef]

36. Lu, J.; Chang, L.; Wang, J.; Sang, L.; Wu, S.; Zhang, Y. In-situ investigation of the anisotropic mechanical properties of laser direct metal deposition Ti6Al4V alloy. *Mater. Sci. Eng. A* **2018**, *712*, 199–205. [CrossRef]

37. Kok, Y.; Tan, X.P.; Wang, P.; Nai, M.L.; Loh, N.H.; Liu, E.; Tor, S.B. Anisotropy and heterogeneity of microstructure and mechanical properties in metal additive manufacturing: A critical review. *Mater. Des.* **2018**, *139*, 565–586. [CrossRef]

38. Chen, S.; Tan, Q.; Gao, W.; Wu, G.; Fan, J.; Feng, Z.; Huang, T.; Godfrey, A.W.; Zhang, M.; Huang, X. Effect of heat treatment on the anisotropy in mechanical properties of selective laser melted AlSi10Mg. *Mater. Sci. Eng. A* **2022**, *858*, 144130. [CrossRef]

39. Dixit, S.; Liu, S.; Murdoch, H.A.; Smith, P.M. Investigating build orientation-induced mechanical anisotropy in additive manufacturing 316L stainless steel. *Mater. Sci. Eng. A* **2023**, *880*, 145308. [CrossRef]

40. Ricci, S.; Zucca, G.; Iannitti, G.; Ruggiero, A.; Sgambetterra, M.; Rizzi, G.; Bonora, N.; Testa, G. Characterization of Asymmetric and Anisotropic Plastic Flow of L-PBF AlSi10Mg. *Exp. Mech.* **2023**, *63*, 1409–1425. [CrossRef]

41. Cain, V.; Thijs, L.; Van Humbeeck, J.; Van Hooreweder, B.; Knutsen, R. Crack propagation and fracture toughness of Ti6Al4V alloy produced by selective laser melting. *Addit. Manuf.* **2015**, *5*, 68–76. [CrossRef]

42. Al-Maharma, A.Y.; Patil, S.P.; Markert, B. Effects of porosity on the mechanical properties of additively manufactured components: A critical review. *Mater. Res. Express* **2020**, *7*, 122001. [CrossRef]

43. Guzanová, A.; Ižaríková, G.; Brezinová, J.; Živčák, J.; Draganovská, D.; Hudák, R. Influence of build orientation, heat treatment, and laser power on the hardness of Ti6Al4V manufactured using the DMLS process. *Metals* **2017**, *7*, 318. [CrossRef]

44. Al-Rubaie, K.S.; Melotti, S.; Rabelo, A.; Paiva, J.M.; Elbestawi, M.A.; Veldhuis, S.C. Machinability of SLM-produced Ti6Al4V titanium alloy parts. *J. Manuf. Process.* **2020**, *57*, 768–786. [CrossRef]

45. Hall, E.O. Variation of Hardness of Metals with Grain Size. *Nature* **1954**, *173*, 948–949. [CrossRef]

46. Lee, W.S.; Lin, M.T. The effects of strain rate and temperature on the compressive deformation behaviour of Ti-6Al-4V alloy. *J. Mater. Process. Technol.* **1997**, *71*, 235–246. [CrossRef]

47. Nixon, M.E.; Cazacu, O.; Lebensohn, R.A. Anisotropic response of high-purity α-titanium: Experimental characterization and constitutive modeling. *Int. J. Plast.* **2010**, *26*, 516–532. [CrossRef]

48. Lin, P.; Hao, Y.; Zhang, B.; Zhang, S.; Chi, C.; Shen, J. Tension–compression asymmetry in yielding and strain hardening behavior of CP-Ti at room temperature. *Mater. Sci. Eng. A* **2017**, *707*, 172–180. [CrossRef]

49. Syed, F.W.; Anil Kumar, V.; Gupta, R.K.; Kanjarla, A.K. Role of microstructure on the tension/compression asymmetry in a two-phase Ti-5Al-3Mo-1.5V titanium alloy. *J. Alloys Compd.* **2019**, *795*, 151–162. [CrossRef]

50. Suryawanshi, J.; Singh, G.; Msolli, S.; Jhon, M.H.; Ramamurty, U. Tension–compression asymmetry and shear strength of titanium alloys. *Acta Mater.* **2021**, *221*, 117392. [CrossRef]
51. Neeraj, T.; Savage, M.F.; Tatalovich, J.; Kovarik, L.; Hayes, R.W.; Mills, M.J. Observation of tension–compression asymmetry in α/β and titanium alloys. *Philos. Mag.* **2005**, *85*, 279–295. [CrossRef]
52. Gilles, G.; Hammami, W.; Libertiaux, V.; Cazacu, O.; Yoon, J.H.; Kuwabara, T.; Habraken, A.M.; Duchêne, L. Experimental characterization and elasto-plastic modeling of the quasi-static mechanical response of TA-6 v at room temperature. *Int. J. Solids Struct.* **2011**, *48*, 1277–1289. [CrossRef]
53. Tuninetti, V.; Gilles, G.; Milis, O.; Pardoen, T.; Habraken, A.M. Anisotropy and tension–compression asymmetry modeling of the room temperature plastic response of Ti-6Al-4V. *Int. J. Plast.* **2015**, *67*, 53–68. [CrossRef]
54. Singh, P.K.; Kumar, S.; Jain, P.K.; Dixit, U.S. Effect of Build Orientation on Metallurgical and Mechanical Properties of Additively Manufactured Ti-6Al-4V Alloy. *J. Mater. Eng. Perform.* **2024**, *33*, 3476–3493. [CrossRef]
55. Xie, Z.; Dai, Y.; Ou, X.; Ni, S.; Song, M. Effects of selective laser melting build orientations on the microstructure and tensile performance of Ti-6Al-4V alloy. *Mater. Sci. Eng. A* **2020**, *776*, 139001. [CrossRef]
56. Amsterdam, E.; Kool, G.A. High cycle fatigue of laser beam deposited Ti-6Al-4V and inconel 718. In *ICAF 2009, Bridging the Gap between Theory and Operational Practice—Proceedings of the 25th Symposium of the International Committee on Aeronautical Fatigue, Rotterdam, The Netherlands, 27–29 May 2009*; Springer: Dordrecht, The Netherlands, 2009; pp. 1261–1274. [CrossRef]
57. Jaber, H.; Kónya, J.; Kulcsár, K.; Kovács, T. Effects of Annealing and Solution Treatments on the Microstructure and Mechanical Properties of Ti6Al4V Manufactured by Selective Laser Melting. *Materials* **2022**, *15*, 1978. [CrossRef]
58. Wang, L.; Ma, C.; Huang, J.; Ding, H.Y.; Chu, M.Q. Microstructure and tensile properties of Ti-6Al-4V alloys manufactured by selective laser melting with optimized processing parameters. *IOP Conf. Ser. Mater. Sci. Eng.* **2017**, *265*, 012015. [CrossRef]
59. Carroll, B.E.; Palmer, T.A.; Beese, A.M. Anisotropic tensile behavior of Ti-6Al-4V components fabricated with directed energy deposition additive manufacturing. *Acta Mater.* **2015**, *87*, 309–320. [CrossRef]
60. Sun, W.; Ma, Y.; Huang, W.; Zhang, W.; Qian, X. Effects of build direction on tensile and fatigue performance of selective laser melting Ti6Al4V titanium alloy. *Int. J. Fatigue* **2020**, *130*, 105260. [CrossRef]
61. Chong, Y.; Bhattacharjee, T.; Yi, J.; Shibata, A.; Tsuji, N. Mechanical properties of fully martensite microstructure in Ti-6Al-4V alloy transformed from refined beta grains obtained by rapid heat treatment (RHT). *Scr. Mater.* **2017**, *138*, 66–70. [CrossRef]
62. Hockett, J.E.; Sherby, O.D. Large strain deformation of polycrystalline metals at low homologous temperatures. *J. Mech. Phys. Solids* **1975**, *23*, 87–98. [CrossRef]
63. Cao, S.; Chu, R.; Zhou, X.; Yang, K.; Jia, Q.; Lim, C.V.S.; Huang, A.; Wu, X. Role of martensite decomposition in tensile properties of selective laser melted Ti-6Al-4V. *J. Alloys Compd.* **2018**, *744*, 357–363. [CrossRef]
64. Mouritz, A.P. *Introduction to Aerospace Materials*; Elsevier: Amsterdam, The Netherlands, 2012.
65. Ivanov, S.; Gushchina, M.; Artinov, A.; Khomutov, M.; Zemlyakov, E. Effect of elevated temperatures on the mechanical properties of a direct laser deposited ti-6al-4v. *Materials* **2021**, *14*, 6432. [CrossRef]
66. Lennon, A.M.; Ramesh, K.T. The influence of crystal structure on the dynamic behavior of materials at high temperatures. *Int. J. Plast.* **2004**, *20*, 269–290. [CrossRef]
67. Gao, C.Y.; Zhang, L.C.; Yan, H.X. A new constitutive model for HCP metals. *Mater. Sci. Eng. A* **2011**, *528*, 4445–4452. [CrossRef]
68. Tvergaard, V.; Needleman, A. Analysis of the cup-cone fracture in a round tensile bar. *Acta Metall.* **1984**, *32*, 157–169. [CrossRef]
69. Lavogiez, C.; Dancette, S.; Cazottes, S.; Le Bourlot, C.; Maire, E. In situ analysis of plasticity and damage nucleation in a Ti-6Al-4V alloy and laser weld. *Mater. Charact.* **2018**, *146*, 81–90. [CrossRef]